cury is nearly zero. In (1), Harmon and Slade argue that the Arecibo observations further constrain the pole direction fortuitously along the direction of greatest uncertainty in Klaasen's 50% error ellipse (but not reducing the 2.5° error in the orthogonal direction).
22. B. Hapke, *Icarus* **88**, 407 (1990); ____ and D. Blewitt, *Nature* **352**, 46 (1991).
23. K. J. Peters, *Phys. Rev. B* **46** (no. 2), 801 (1992).
24. Unit 1 in figure 1 of K. E. Herkenhoff and B. C. Murray, *J. Geophys. Res.* **95**, 1343 (1990).
25. T. W. Thompson, *Moon* 10, 51 (1974).
26. S. H. Zisk, G. H. Pettengill, G. W. Catuna, *ibid.*, p. 17.
27. T. W. Thompson, S. H. Zisk, R. W. Shorthill, P. H. Schultz, J. A. Cutts, *Icarus* **46**, 201 (1981).
28. A. E. Potter and T. H. Morgan, *Science* **248**, 835 (1990); see also R. M. Killen, A. E. Potter, T. H. Morgan, *Icarus* **85**, 145 (1990).
29. A. L. Sprague, R. W. H. Kozlowski, D. M. Hunten, *Science* **249**, 1140 (1990). See also A. L. Sprague, *Icarus* **84**, 93 (1990); R. M. Killen, A. E. Potter, T. H. Morgan, *Science* **252**, 974 (1991); A. L. Sprague, R. W. H. Kozlowski, D. M. Hunten, *ibid.*, p. 975.
30. D. O. Muhleman, *Astron. J.* **69**, 34 (1964).
31. We thank the observing staff at the VLA and the Radio Astronomy and Radar Group at Goldstone for the attention and care in performing the experiments. In particular we thank K. Sowinski and W. M. Goss for their help in various aspects of these experiments. R. F. Jurgens, E. M. Standish, Jr., and D. K. Yeomans provided assistance with radar operations and ephemerides. We also thank D. A. Paige, S. E. Wood, A. R. Vasavada, and J. K. Harmon for discussions of their results before publication. Part of the research described above was carried out at the Jet Propulsion Laboratory, California Institute of Technology, under a contract with the National Aeronautics and Space Administration. The Caltech work was supported under NASA grant NAGW 1499. Contribution number 5158 from the Division of Geological and Planetary Sciences, Caltech.

3 June 1992; accepted 4 August 1992

Radar Mapping of Mercury: Full-Disk Images and Polar Anomalies

J. K. Harmon and M. A. Slade

A random-code technique has been used at Arecibo to obtain delay-Doppler radar images of the full disk of Mercury. Anomalously bright features were found at the north and south poles. The north polar feature is oblong (4° by 8°) and offset from the pole. The smaller south polar feature is mostly confined to the floor of the crater Chao Meng-Fu. The polar locations and radar properties of these features indicate that they may be produced by volume scattering in ice. The images also reveal a variety of more subdued reflectivity features ranging in size from hundreds to thousands of kilometers; some of these appear to have an impact origin.

Radar reflectivity mapping of Mercury has been limited in the past to delay-Doppler imaging of the polarized echo (1) in the near-subradar region (2, 3). Full-disk imaging and depolarized imaging of the planet have been deterred by problems such as low echo strength and "overspreading" (4). Recent advances have been made in overcoming these limitations with the use of synthesis mapping between Goldstone and the Very Large Array (VLA) (5) and random-code delay-Doppler mapping at Arecibo. The new full-disk radar images obtained at these facilities have revealed several interesting radar features of Mercury, most notably the anomalous bright spots at the north and south poles. Here we present some of the new Arecibo results.

The mapping observations were made on a total of 28 dates during three separate periods near inferior conjunction: 28 March to 21 April 1991, 31 July to 29 August 1991, and 14 to 29 March 1992. The subradar track during the spring 1991 observations went from (in planetocentric, or longitude/latitude, coordinates) 285°W, 5.3°S to 79°W, 3.6°S. For the summer 1991 observations the track went from 205°W, 9.2°N to 33°W, 9.5°N and reached a northernmost latitude of 11.6°N. Following the success of the 1991 observations, the March 1992 dates were added to give a better view of the south polar anomaly; the track for these observations went from 301°W, 7.1°S to 40°W, 7.4°S.

The observations were made with the Arecibo S-band (λ = 12.6 cm) radar transmitting a 420-kW, circularly polarized wave. The transmitted wave was modulated by a nonrepeating binary phase code with a 100-μs baud. The received signal for each orthogonal circular polarization was filtered, sampled, and processed in precisely the same way as for recent random-code mapping observations of Mars (6) except that a longer Fourier transform (8192 elements) was used to achieve a Doppler resolution of 1.22 Hz. The random-code method works on the principle that, by using a nonrepeating code, one can turn what would otherwise be a confusing aliasing of the overspread echo into an additive white-noise clutter (7). This clutter component contributes less than 15% of the total noise background for the depolarized echo.

Each day's data were reduced to a single delay-Doppler array formed from the sum of one to three observing runs; each run had an integration time of 9 to 13 min. After estimating and subtracting a noise base line, we constructed a radar reflectivity map (image) from the delay-Doppler array. The mapping was done by construction of a 512 by 512 square array of pixels circumscribing the projected disk of Mercury. A mapping from delay-Doppler to Cartesian coordinates was done and a value representing the radar reflectivity (cross section per unit projected area) was assigned to each pixel. The image was then smoothed to an effective resolution of 5 by 3 pixels to reduce noise. Radar images made with this technique have a north-south ambiguity about the Doppler equator. We have been able to resolve the ambiguity for most of the prominent reflectivity features by comparing images obtained at different aspects. The spurious component of any given ambiguous feature pair can be identified because its mapped planetocentric position changes with aspect while the true feature remains fixed. Even small changes in subradar latitude can suffice to resolve some mapping ambiguities by eye.

Figures 1 and 2 show two sets of depolarized images obtained at northern and southern latitudes, respectively. The images are dominated by a pair of mid-latitude bright patches in the north and south at about 350°W longitude. These features are located in the hemisphere (190° to 10°W) that was not imaged by Mariner 10. The northern patch is centered at 345°W, 55°N, and the southern patch is at 348°W, 30°S. Unfortunately, the position of the Doppler equator in Fig. 1 is such that the northern and southern features are largely folded over each other (although closer inspection reveals the true location of the brightest spot in the northern feature). The two features separate out in the more southerly images (Fig. 2); the southern feature dominates, whereas the northern feature appears only as a faint patch in the far north (Fig. 2B). This change in the relative brightness of the two features is apparently an incidence-angle effect. These two features together account for one of the two depolarized enhancements seen by Goldstein (8) in continuous-wave Doppler spectra. The large equatorial bright area east of 270°W in Fig. 1A probably corresponds to Goldstein's other depolarized enhancement. Both of the 350°W mid-latitude features have reflectivities of about 0.020, which corresponds to a fivefold enhancement over the planet average. Such reflectivities and enhancement factors are reminiscent of depolarized bright spots on the

J. K. Harmon, National Astronomy and Ionosphere Center, Arecibo, PR 00613.
M. A. Slade, Jet Propulsion Laboratory, California Institute of Technology, Pasadena, CA 91109.

moon (9, *10*). Most of the lunar features are associated with the floors and ejecta blankets of fresh impact craters, and these two Mercury features may be impact structures as well. The features are much weaker than the depolarized enhancements on Mars, most of which appear to be associated with rough surfaces on volcanoes and lava flows (6, *11*).

The hemisphere (10° to 190°W) imaged by Mariner 10 begins just to the west of the two mid-latitude features. Centered near 33°W, 9°S (Fig. 1B), around the bright-rayed crater Kuiper, is an irregular bright patch with a reflectivity of 0.010. Such lunar craters as Tycho (*12*) show rays and other radar-bright features, and the Kuiper feature is probably analogous to these. Images (not shown here) obtained farther to the west show another radar-bright feature (reflectivity = 0.015) that may correspond to Copley, another prominent bright-rayed crater.

One interesting feature that is not an impact structure is the large, kidney-shaped, radar-dark patch seen near the equator at about 300°W (Fig. 2A). Comparison of images from April 1991 to those of March 1992 indicates that this is primarily a northern hemispheric feature. Although it is located in the unimaged hemisphere of Mariner 10, we do know from Arecibo radar altimetry (*13*) that this feature coincides precisely with the location of a 2.5-km-high plateau. Unpublished high-resolution radar images from Arecibo show that this plateau is heavily cratered, whereas the lower region just to the east has a smooth appearance. This craterless region to the east, which is radar-bright in the depolarized images, must be smooth plains or intercrater plains. Apparently some resurfacing process has left this low-lying region with a rougher or denser surface while leaving the adjacent plateau untouched.

The most interesting result is the identification of anomalously bright features at the north and south poles of Mercury. The north polar feature was first discovered in a Goldstone-VLA radar map from 8 August 1991 (5). It was subsequently identified in all of the Arecibo random-code mapping data obtained between 31 July and 29 August 1991. Soon after this a south polar bright spot was found in Arecibo random-code maps from the earlier (more southerly) observations from March to April 1991. This south polar feature was confirmed and its position refined by the March 1992 observations.

The north polar anomaly is the brightest feature in Fig. 1. The north-south ambiguity is easily resolved by comparing Figs. 1 and 2 (if this were a southern feature, it would have shown up strongly near latitude 65°S in Fig. 2). The average reflectivity of this feature is 0.10, and some parts are as bright as 0.14. It also shows up in the polarized echo, and we estimated $\mu_c = 1.01 \pm 0.15$ (90% confidence) for the ratio of depolarized to polarized power. The north polar anomaly is oblong, measuring approximately 4° by 8°. Although this feature includes the pole, its centroid is offset from it by about 2°. Both the long axis and the offset are approximately aligned along the 300°W longitude meridian. The feature is shown end-on in Fig. 1A and from a broadside aspect in Fig. 1B. Both its shape and its

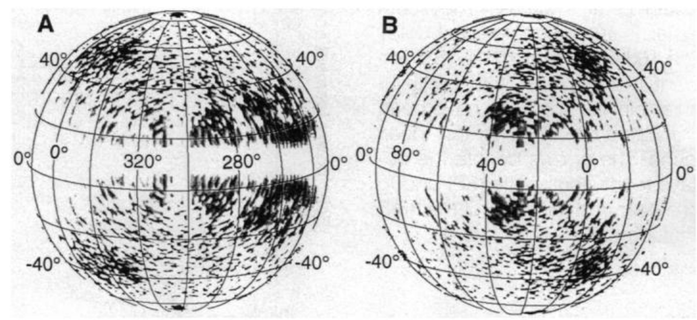

Fig. 1. Depolarized radar reflectivity images of Mercury from (**A**) 16 August 1991 (subradar point at 304.2°W, 11.6°N) and (**B**) 28 August 1991 (subradar point at 26.6°W, 9.9°N). Darker shades denote higher reflectivity. The darkest shades correspond to reflectivities in excess of 0.020 in (A) and 0.015 in (B). The polar region has been scaled to 30% of its true reflectivity to reduce the dynamic range of the image. A strip 10° wide has been blanked out along the Doppler equator where the delay-Doppler mapping is ill-defined.

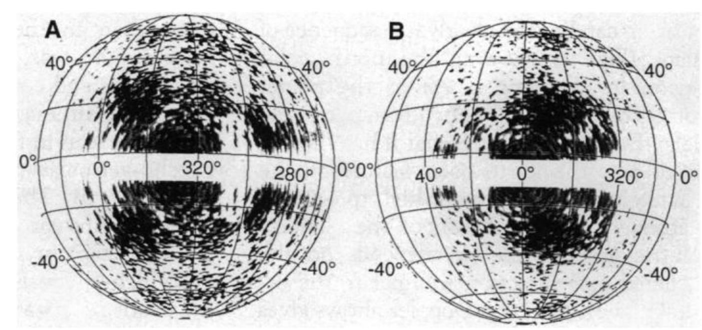

Fig. 2. Depolarized images from (**A**) 4 April 1991 (subradar point at 325.2°W, 5.5°S) and (**B**) 23 March 1992 (subradar point at 358.5°W, 7.8°S). In both images the darkest shades correspond to reflectivities in excess of 0.017. The polar region has been scaled to (A) 30% or (B) 50% of its true reflectivity to reduce the dynamic range of the image.

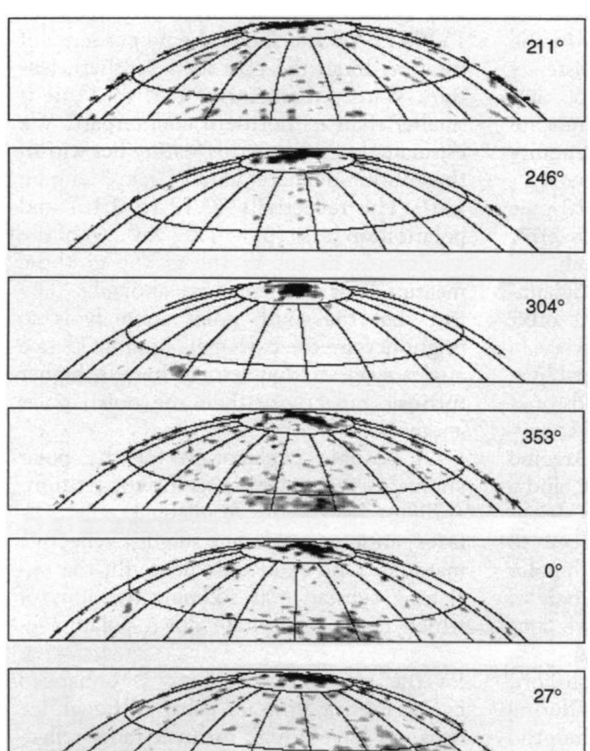

Fig. 3. Sequence of images of the north polar region showing the north polar anomaly at six rotational phases during the period 1 to 28 August 1991. The grids show longitude and latitude at 20° intervals; the topmost latitude circle is at 80°N. The numbers give the central (subradar) longitude meridian for each image.

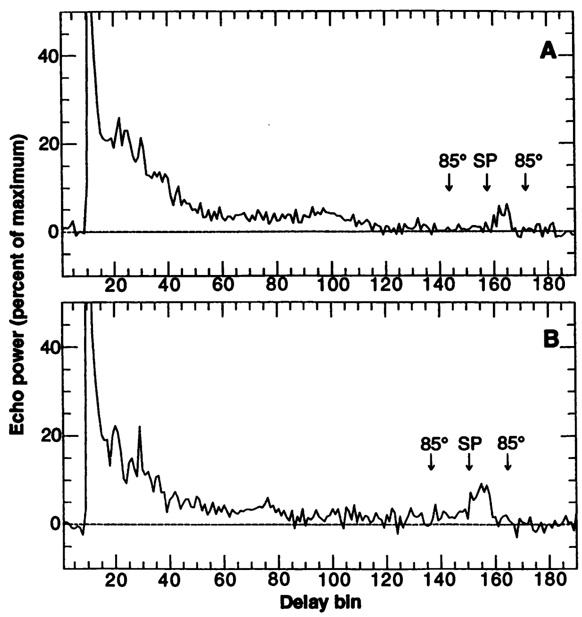

Fig. 4. Plots of depolarized echo power versus time delay for (**A**) 7 April 1991 (subradar point at 343.8°W, 5.5°S) and (**B**) 23 March 1992 (subradar point at 358.5°W, 7.8°S). The power has been summed over a narrow Doppler strip containing echo from the south polar anomaly. The south polar feature is centered at delay bin 163 in (A) and 154 in (B). The front of the planet can be seen near bin 10. The plots have been truncated at 50% of the peak echo. The arrows denote the delays to the south pole (SP) and to the near and far sides of the 85°S latitude circle.

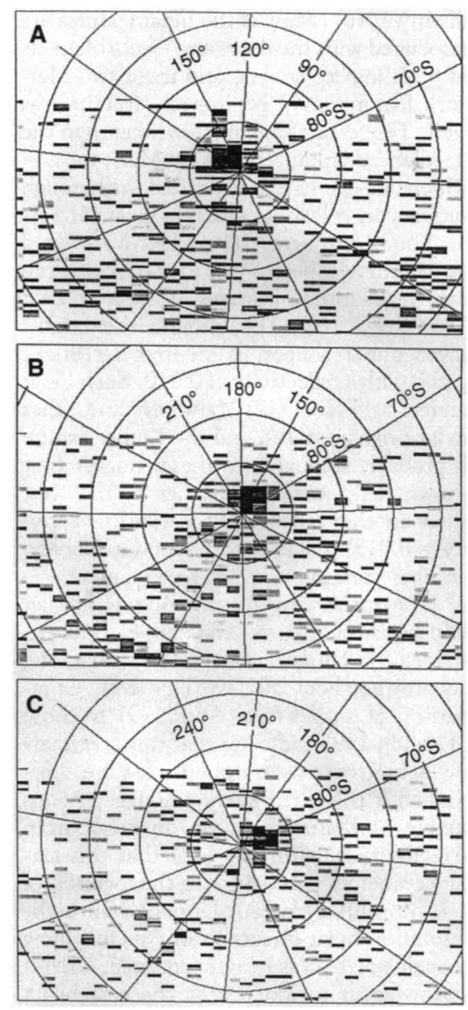

Fig. 5. Radar images of the south polar region at three rotational phases. Data are from (**A**) 14 and 15 March 1992, (**B**) 23 March 1992, and (**C**) 28 and 29 March 1992. The rectangular cells correspond to the raw (unsmoothed) pixels normalized to cross section per unit surface (not projected) area. Radar illumination is from the bottom, with the blank area at top corresponding to the region hidden beyond the radar horizon.

position can be seen clearly in a sequence of maps (Fig. 3) showing the north polar region in changing aspect as the planet rotates by nearly 180°. An advantage of the delay-Doppler method is that it has allowed us to map the north polar feature on the planetocentric grid with high precision. Although the orientation of the planetocentric grid on the sky depends on the assumed pole direction (normal to the orbital plane), the echo Doppler always gives the true transverse distance of a feature from the apparent rotation axis regardless of the assumed pole. This means that our estimate of the offset of this feature from the pole (Fig. 3) is insensitive to errors in the assumed pole direction. Also, consistency checks of the feature's mapped location with its changing rotational aspect indicate that the component of the polar obliquity in the line-of-sight direction must be <1°. For comparison, the best Mariner 10 pole direction estimate (*14*) has a 50% error ellipse whose long axis (roughly aligned with both our line of sight and the dynamically significant line containing the orbit and ecliptic normals) measures 13°.

The south polar region was not visible at the time of the Arecibo and Goldstone-VLA observations in August 1991. However, it was barely visible during the Arecibo observations in March to April 1991, and a polar feature was identified in the delay-Doppler arrays from four dates between 28 March and 7 April. Because the north polar anomaly should have been hidden behind the northern limb on these dates, we concluded that this feature was coming from the south pole. To confirm this conclusion, we made observations on nine dates during the period 14 to 29 March 1992, when the subradar track was as much as 2.3° farther south than in the previous spring. The polar feature was seen again on each of these dates and confirmed as coming from the south. Although the south polar anomaly can be seen in Fig. 2, it shows up better in echo-versus-delay plots (Fig. 4) and polar views (Fig. 5). The polar feature comes in ten delay bins earlier (relative to the planet's front cap) in 1992 than in 1991 (Fig. 4), which is consistent with the fact that the south pole was tilted toward us by an extra 2.3° in 1992. During the March 1992 observations we were able to follow the south polar feature as the planet rotated by 100° (Fig. 5). This feature is centered near 150°W, 88°S and shows the proper sense of rotation about the pole for a southern feature. With a diameter of 2.5° to 3°, it is smaller than its northern counterpart. We estimate that most of this feature lies within the 150-km-diameter crater Chao Meng-Fu (*15*). The reflectivity (0.10 to 0.16) and polarization ratio ($\mu_c = 1.07 \pm 0.20$) of the south polar anomaly are similar to those measured for the northern anomaly. The fact that the south polar anomaly is so bright despite the extremely high incidence angles suggests that it may have a higher intrinsic reflectivity than the north polar anomaly.

A possible explanation for the polar anomalies is that we are seeing conventional diffuse backscatter from rough polar surfaces enriched in some highly reflective material. One exotic candidate for the enriching substance is sodium, the ions of which could precipitate down polar magnetic field lines (*16*). A more likely reason for the polar radar features is enhanced backscattering from ice caps. Although ice does not have a high intrinsic radar reflectivity, it could serve as the low-loss matrix material required by volume-scattering mechanisms such as coherent backscattering (*17*). A strong precedent for the Mercury ice hypothesis is provided by the fact that high radar reflectivities and high μ_c values have been measured for the icy Galilean satellites and the south residual icecap of Mars. The suggestion that there may be ice on Mercury is a startling one prima facie. However, both hydrogen and oxygen have been detected in the Mercurian atmosphere and photolysis of water vapor has been suggested as a possible source of hydrogen (*18*). Recent thermal modeling work (*19*) suggests that water ice could exist in a stable state near the planet's poles. The location of the south polar anomaly in the floor of a large polar crater is consistent with the ice theory (or any theory based on low polar temperatures) because most of the crater floor would be in perpetual shadow.

REFERENCES AND NOTES

1. For circularly polarized transmission, the polarized echo is the component returned in the circular polarization orthogonal to the transmitted sense; the depolarized echo is the component returned in the same polarization sense. The polarized echo is normally dominated by quasi-specular reflection from large planar facets in the near-subradar region. The depolarized echo can be associated with diffuse reflection from wavelength-scale roughness elements, multiple scattering, or subsurface scattering in icy regoliths.
2. S. Zohar and R. M. Goldstein, *Astron. J.* **79**, 85 (1974).
3. P. E. Clark, M. A. Leake, R. F. Jurgens, in *Mercury*, F. Vilas, C. R. Chapman, M. S. Matthews, Eds. (Univ. of Arizona Press, Tucson, 1988), pp. 77–100.
4. A radar target is said to be "overspread" when the product $B\tau$ of its rotational Doppler bandwidth B and delay depth τ exceeds unity. Conventional delay-Doppler mapping uses a repetitive code with a cycle time greater than τ. Because the sampling interval for the spectral (Doppler) analysis is equal to the code cycle time, the echo from an overspread target will be aliased in Doppler. Mercury is overspread by up to 75% at S-band wavelengths and 270% at X-band wavelengths.
5. M. A. Slade, B. J. Butler, D. O. Muhleman, *Science* **258**, 635 (1992).
6. J. K. Harmon, M. P. Sulzer, P. J. Perillat, J. F. Chandler, *Icarus* **95**, 153 (1992).
7. The decoding for a given delay bin is done by multiplication of the echo signal by an appropriately lagged replica of the transmitted code. The uncorrelated product of the code and the echo from other delays constitutes a random "clutter" that adds to the total noise background. For more on this coding technique, see M. P. Sulzer [*Radio Sci.* **21**, 1033 (1986)].
8. R. M. Goldstein, *Science* **168**, 467 (1970).
9. G. H. Pettengill and T. W. Thompson, *Icarus* **8**, 457 (1968).
10. T. W. Thompson, *Moon* **10**, 51 (1974).
11. D. O. Muhleman, B. J. Butler, A. W. Grossman, M. A. Slade, *Science* **253**, 1508 (1991).
12. S. H. Zisk, G. H. Pettengill, G. W. Catuna, *Moon* **10**, 17 (1974).
13. J. K. Harmon, D. B. Campbell, D. L. Bindschadler, J. W. Head, I. I. Shapiro, *J. Geophys. Res.* **91**, 385 (1986).
14. K. P. Klaasen, *Icarus* **28**, 469 (1976).
15. M. E. Davies, S. E. Dwornik, D. E. Gault, R. G. Strom, *Atlas of Mercury* (National Aeronautics and Space Administration, Washington, DC, 1978).
16. R. M. Killen, A. E. Potter, T. H. Morgan, *Icarus* **85**, 145 (1990).
17. B. Hapke, *ibid.* **88**, 407 (1990).
18. A. L. Broadfoot, *Rev. Geophys. Space Phys.* **14**, 625 (1976).
19. D. A. Paige, S. E. Wood, A. R. Vasavada, *Science* **258**, 643 (1992).

20. A. Crespo, R. Vélez, J. Cruz, A. Vázquez, P. Perillat, M. Dryer, M. Sulzer, and J. Chandler provided support for the Arecibo observations. We thank the authors of the companion papers (D. Paige, S. Wood, A. Vasavada, B. Butler, and D. Muhleman) for communicating some of their results to us before publication. Part of the research described above was carried out by the Jet Propulsion Laboratory, California Institute of Technology, under contract with the National Aeronautics and Space Administration (NASA). The National Astronomy and Ionosphere Center (Arecibo Observatory) is operated by Cornell University under a cooperative agreement with the National Science Foundation and with support from NASA.

29 May 1992; accepted 20 July 1992

The Thermal Stability of Water Ice at the Poles of Mercury

David A. Paige,* Stephen E. Wood, Ashwin R. Vasavada

Recent radar observations of Mercury have revealed the presence of anomalous radar reflectivity and polarization features near its north and south poles. Thermal model calculations show that, despite Mercury's proximity to the sun, the temperatures of flat, low-reflectivity surfaces at Mercury's poles are not expected to exceed 167 kelvin. The locations of the anomalous polar radar features appear to be correlated with the locations of large, high-latitude impact craters. Maximum surface temperatures in the permanently shadowed regions of these craters are expected to be significantly colder, as low as 60 kelvin in the largest craters. These results are consistent with the presence of water ice, because at temperatures lower than 112 kelvin, water ice should be stable to evaporation over time scales of billions of years.

Over the past three decades, a circumstantial case has developed for the possible stability of water ice deposits in high-latitude, permanently shadowed regions on the moon (*1–3*), but there is no definitive observational evidence for their existence. The possibility that water ice could be cold-trapped at the poles of Mercury has also been suggested (*4*). The new 3.5-cm (*5*) and 12.6-cm (*6*) radar observations of Mercury motivate detailed consideration of the thermal state of the planet's polar regions as well as the long-term sources and sinks of water and other volatiles (*7*). Here we report the results of thermal model calculations that suggest that water ice could be stable to evaporation on Mercury in regions where anomalous radar reflectivity and polarization features are observed.

Using a thermal model, we have calculated the temperatures of flat surfaces on Mercury as a function of latitude, longitude, and season. Because of Mercury's 3/2 resonant rotation rate and eccentric orbit, the distribution of incident solar radiation is a complicated function that repeats every 2 years (*8*). Because of the planet's proximity to the sun, the finite angular size of the sun's disk (*9*) and solar limb darkening are taken into account when the sun's disk intersects the local horizon. Near Mercury's poles, the distribution of incident solar radiation is sensitive to the orientation of the planet's rotation axis relative to its orbital plane. Recent Arecibo radar observations show that Mercury's obliquity is less than 1° (*6*). Dynamical models predict that the most stable configuration of Mercury's spin axis corresponds to Cassini State 1, in which the spin axis is displaced slightly away from the orbit normal vector in a direction that is coplanar with the solar system normal vector and the orbit normal vector (*10*). The magnitude of this displacement is determined by the differences in the principal moments of inertia (*10*). Based on Mariner 10 gravity data (*11*), the present obliquity of Mercury is likely to be ≤0.05° (*10*). In our model, the Cassini State 1 configuration is assumed; in it, northern spring equinox occurs at the ascending node of Mercury's orbit relative to the solar system plane (*12*). The present value of ω, the angle between the ascending node and perihelion, is approximately 29.1° (*13*).

Because Mercury lacks an appreciable atmosphere, we determined the temperatures of flat surfaces using only the net effects of solar and infrared radiation and thermal conduction. Ground-based observations and Mariner 10 data have shown that the average thermal and reflectance properties of the surface of Mercury are similar to those of the moon (*14, 15*). In our model, the solar reflectance of the surface was assumed to be 0.15 and the emissivity of the surface was assumed to be 0.90. At each latitude and longitude, the model solves the one-dimensional heat diffusion equation using the bulk thermal properties of lunar soil, including the expected variation of thermal conductivity and heat capacity with temperature (*16*). In accordance with the results of models for the thermal history of Mercury's interior, the present surface heat flow rate was assumed to be 0.020 W/m^2 (*17*). The general results of the model calculations were consistent with those of earlier studies in that daytime surface temperatures were close to being in instantaneous radiative equilibrium and nighttime surface temperatures were determined by the combined effects of thermal inertia and heat flow (*8, 14*).

Maps of model-calculated, biannual maximum and average temperatures for flat surfaces in the north polar region of Mercury (Fig. 1, A and B) show strong longitudinal dependence. Because noon at perihelion occurs alternately at longitudes of 0° and 180°, polar isotherms tend to be elon-

Department of Earth and Space Sciences, University of California, Los Angeles, Los Angeles, CA 90024.

*To whom correspondence should be addressed.